ORIGINAL PAPER

Enhanced photocatalytic hydrogen production from water–methanol mixture using cerium and nonmetals (B/C/N/S) co-doped titanium dioxide

N. Vinothkumar · Mahuya De

Abstract In the present study, photocatalytic hydrogen production from water/methanol solution was investigated over cerium and nonmetal (B/C/N/S) co-doped titanium dioxide catalyst under visible light irradiation. The cerium and nonmetal co-doped titania photocatalysts were prepared by co-precipitation and characterized by surface area and pore size analysis, X-ray diffraction analysis, diffuse reflectance UV–Vis spectroscopy analysis, and photoluminescence analysis. The UV–Visible spectra showed that incorporation of cerium and nonmetals to TiO_2 resulted in narrow band gap and improved absorption of visible light. The band gap energy of co-doped samples depended on the properties of nonmetals. Photoluminescence studies showed that the radiative recombination rates of photogenerated electron–hole pairs were effectively suppressed by the addition of cerium and nonmetals and contributed to higher activity. The highest hydrogen production of 206 µmol/h was obtained for Ce–N–TiO_2 sample, which can be attributed to the higher surface area, higher absorption of visible light, and higher separation efficiency of electron–hole pairs in Ce–N–TiO_2.

N. Vinothkumar · M. De (✉)
Department of Chemical Engineering, Indian Institute of Technology, Guwahati 781 039, Assam, India
e-mail: mahuya@iitg.ernet.in

Introduction

The energy economy of the world mainly depends on the fossil fuels such as coal, natural gas, and petroleum products. Gradual depletion of fossil fuels and fast-growing energy demand has necessitated to develop alternative fuels, which should also be pollution-free, storable, and economical [1]. Hydrogen is considered as a promising alternative fuel for the future. It has higher energy content and high heating value compared to other fuels such as methane, methanol, gasoline, and diesel [2]. At present, hydrogen is mainly produced by steam reforming of methane or naphtha. Various alternative processes such as electrolysis, thermolysis, thermochemical reactions, photolysis, photoelectro-chemical, photocatalytic, and biochemical processes are being studied for the production of hydrogen. But only few of these methods are efficient and economically viable [3]. The production of hydrogen from water using solar radiation is one of the potential routes to achieve clean, low-cost, and eco-friendly fuel. Several oxide materials, such as TiO_2, Fe_2O_3, ZnO, ZrO_2, $K_4Nb_6O_{17}$, $K_2La_2Ti_3O_{10}$, $BaTi_4O_9$, and Ta_2O_5, have been studied for the photodecomposition of water [4–8]. TiO_2 has been reported to be an excellent photocatalyst for water-splitting reaction. Advantages of TiO_2 include chemical inertness, photostability, and low cost. However, the activity of TiO_2 is limited in UV region because of its wide band gap (3.2 eV). The visible light ($\lambda > 400$ nm) constitutes the major fraction of solar spectrum reaching the earth surface. For better utilization of the sunlight, it is essential to develop stable photocatalytic systems with suitable band gap to absorb most of the solar spectrum. In order to develop an efficient titania-based visible light active photocatalyst, various methods have been reported such as doping with metals and nonmetals, dye

sensitization as well as coupling with other semiconductors [9]. The dopant impurities create additional energy levels within the band gap of titania acting either as donor or acceptor level. An extensive review has been done on visible light activity of titania by Pelaez et al. [10]. Photocatalytic activities of TiO_2 doped with rare earth metals and nonmetals are mostly reported for the degradation of pollutants. Xu et al. [11] investigated various rare earth-doped TiO_2 samples for the degradation of nitrite and observed an enhanced photoabsorption in the visible light region. Ce-doped TiO_2 materials were also reported to show high activity under visible light irradiation for photocatalytic degradation of dye and phenol derivatives [12–14]. The $N–TiO_2$ [15], and $S–TiO_2$ [16] were studied for the photodegradations of methylene blue under UV/Visible light irradiation, while $C–TiO_2$ [17] was reported to be active for the degradation of phenol. The titania co-doped with rare earth metals and nitrogen are also reported to show an enhanced activity for the decomposition of pollutants [18, 19]. Though doped TiO_2 catalysts were extensively investigated for the degradation of pollutants, comparatively fewer studies have been reported for photocatalytic hydrogen production [20–22]. In this study, the photocatalytic activities of TiO_2 co-doped with cerium and nonmetals were studied for hydrogen evolution from water–methanol mixture under visible light irradiation. The effect of various nonmetals such as B, C, N, and S on hydrogen production was studied. The physical and optical properties of the photocatalysts affecting the activity were investigated using various characterization techniques such as surface and pore analysis, XRD, UV–Vis, and photoluminescence spectroscopy.

Experimental

Preparation of photocatalyst

Cerium and nonmetal co-doped TiO_2 samples were prepared by co-precipitation method. Titanium tetra isopropoxide (TTIP) and cerium nitrate hexahydrate were used as precursors for titania and ceria, respectively, and were obtained from Sigma-Aldrich. The boric acid, glucose, urea, and thiourea were used as sources for boron, carbon, nitrogen, and sulfur, respectively, and were procured from Merck. The isopropanol and ammonia solution were also procured from Merck.

Requisite amount of TTIP was mixed with isopropanol under continuous stirring condition for 10 min to form solution A. Solution B was prepared by dissolving the required amount of cerium nitrate hexahydrate and respective precursors of nonmetals in deionized water. The loadings in co-doped samples for Ce and nonmetals were

2.5 and 1 mol% of titanium, respectively. The loadings of Ce (x) and nonmetals (y) are defined as

$$x = \frac{Ce(mol)}{Ti(mol)} \times 100 = 2.5 \text{ mol}\% \quad \text{and}$$

$$y = \frac{NM(mol)}{Ti(mol)} \times 100 = 1 \text{ mol}\%.$$

Aqueous ammonia (25 wt%) and solution B were simultaneously added dropwise to the solution A with continuous stirring. Addition of ammonia was continued until complete precipitation occurred. The resultant mixture was stirred for 2 h at room temperature and was placed in a water bath at 363 K for overnight. The precipitate was filtered and dried in an oven at 373 K for 24 h. The as-prepared samples were calcined at 723 K for 3 h. In text, nonmetal co-doped samples are referred as Ce–NM–TiO_2 (NM = B, C, N, S). For reference, cerium-doped titania were prepared by dissolving required amount of cerium nitrate hexahydrate in deionized water (solution B). The amount of Ce was 2.5 mol% of Ti, and sample is represented as Ce–TiO_2 in text. The solution B was added to solution A along with aqueous ammonia as described earlier to obtain cerium-doped titania samples. Similar aging condition and calcination temperature were maintained for the preparation of Ce–TiO_2 sample. Undoped titania was also prepared for reference by similar procedure without the addition of cerium or nonmetals and represented by TiO_2 in text.

Characterization of photocatalyst

The surface areas of the samples were determined from N_2 isotherms collected at 77 K using a Beckman Coulter SA^{TM} 3100 analyzer. Prior to the experiments, the samples were degassed at 423 K for a period of 2 h. The pore size distribution of the photocatalysts was determined by Barrett–Joyner–Halenda (BJH) method. The X-ray diffraction (XRD) patterns were recorded on a Bruker D2 phaser X-ray diffractometer using Ni-filtered Cu K_α as radiation source ($\lambda = 1.5406$ Å) in the 2θ range from 20 to 80° at a scanning rate of 1°/min. A beam voltage and beam current of 40 kV and 40 mA were used, respectively. The diffuse reflectance UV–vis spectra of the photocatalysts were measured on a PerkinElmer Lambda 750 instrument with a 60-mm labsphere specular reflectance accessory at room temperature. The baseline correction was done using a calibrated sample of barium sulfate as reference. The scan parameter was set with slit size 2 nm and scan in the spectral range of 250–650 nm. The photoluminescence (PL) measurements were taken in a Thermo Spectronic (Aminco Bowman Series 2) instrument with a Xe lamp as the excitation source at room temperature. The powders were dispersed in ethanol, and the emission spectra were

collected at an excitation wavelength of 325 nm. The same quantity was used for recording the PL spectra of all the samples. The entrance and exit slit widths were fixed as same for all the measurements. Field emission scanning electron microscopic analysis was done using instrument of ZEISS-Sigma. For FESEM analysis, the samples were dispersed in a solvent and deposited in an aluminum foil that was mounted on a sample holder for gold coating. The composition of the samples was determined by EDS analysis (energy-dispersive X-ray spectroscopy) equipped with SEM instrument (LEO 1430 VP).

Photocatalytic activity studies

The activities of the photocatalysts were examined using the experimental setup shown in Fig. 1. The reaction was typically carried out by adding 0.2 g catalyst to solution of water (25 ml) and methanol (1 ml) under stirred condition. Prior to irradiation, the reaction mixture was de-aerated with N_2 gas (50 ml/min) for 30 min to completely remove the dissolved oxygen. Then, the reaction mixture was irradiated with a 500-W tungsten halogen lamp (Halonix, India), placed approximately 15 cm away from the reactor, as source of visible light. The emission spectrum of the lamp was measured in front of the reactor using Ocean optics USB4000 spectrometer as shown in Figure S1 in the

supplementary information. The temperature of the reaction mixture was maintained at 307 K using a water circulation bath, which also acted as an IR filter. The evolved gas was collected in an inverted burette by water displacement method. The gas mixture was analyzed using a gas chromatograph (Varian, CP 3800) equipped with carbosieve SII column and thermal conductivity detector. After completion of the photocatalytic reaction, the liquid solution was analyzed for the detection of intermediates (formaldehyde and formic acid) by HPLC (SHIMADZU, C18 column). To confirm the photocatalytic activity of the catalysts, experiments were conducted first in the absence of light with catalysts and next in the presence of light without catalyst. In both cases, no hydrogen evolution was observed. The hydrogen evolution was observed only when the reaction was carried out in the presence of both light and catalyst. In all cases, same feed mixture was used. This confirmed the photocatalytic activity of the catalysts.

Results and discussion

Characterization of prepared catalysts

The actual composition of the prepared photocatalysts was determined by EDS, and the results are shown in Table S1

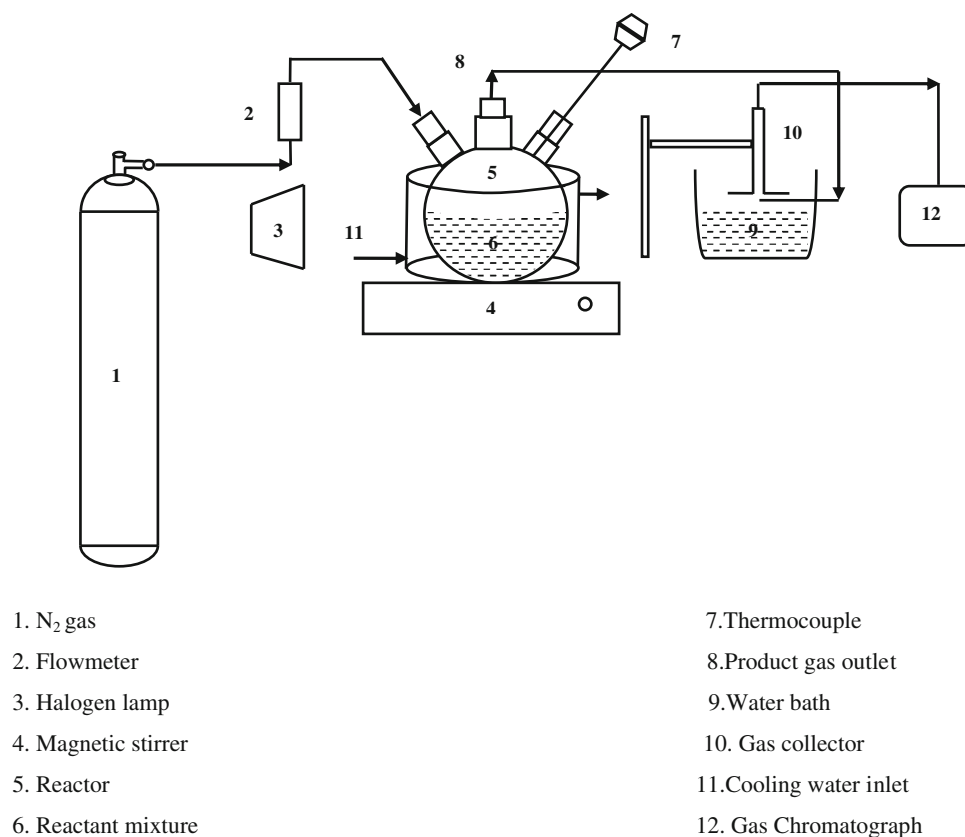**Fig. 1** Schematic representation of experimental setup for photocatalytic water splitting

1. N_2 gas
2. Flowmeter
3. Halogen lamp
4. Magnetic stirrer
5. Reactor
6. Reactant mixture

7. Thermocouple
8. Product gas outlet
9. Water bath
10. Gas collector
11. Cooling water inlet
12. Gas Chromatograph

Table 1 Physicochemical and crystalline properties of undoped TiO_2, Ce–TiO_2, and Ce–NM–TiO_2 (NM = B, C, N, S) samples

Samples	BET surface area (m^2/g)	Pore volume (cc/g)	Lattice parameters Anatase		Lattice distortion	d spacing (Å)
			a (Å) (101)	c (Å) (004)		
TiO_2	84	0.45	3.7435	9.4217	0.378	3.4790
Ce–TiO_2	70	0.36	3.7451	9.4599	0.268	3.4822
Ce–B–TiO_2	87	0.57	3.7907	9.5197	0.271	3.5128
Ce–C–TiO_2	53	0.67	3.7659	9.5080	0.387	3.5013
Ce–N–TiO_2	158	0.06	3.7936	9.7181	0.301	3.2240
Ce–S–TiO_2	39	0.18	3.7727	9.7014	1.391	3.5174

of supplementary information. The actual cerium content in samples varied in the range of 2.39–2.49 mol%, and nonmetal content varied in the range of 0.8–0.97 mol% (Table S2 of supplementary information). Thus, the actual composition agreed well with the intended composition of the photocatalysts within experimental error.

The surface area and pore volumes of undoped TiO_2, Ce–TiO_2, Ce–NM–TiO_2 (NM = B, C, N, S) samples are shown in Table 1. Surface area and pore volume of titania decreased with the addition of ceria. Structure modification and partial pore blockage in the presence of cerium may be responsible for decrease in surface area and pore volume in cerium-doped samples. The isotherm of Ce–TiO_2 and corresponding pore size distribution are shown in Fig. 2a. The Ce–TiO_2 sample exhibited a type IV isotherm with a H1-type hysteresis loop associated with open-ended cylindrical pores. The pore size distribution of Ce–TiO_2 showed the presence of both mesopores and macropores with pore diameter in the range of 3–148 nm. Co-doping of titania with nonmetals along with cerium resulted in increase in surface area as shown in Table 1. The co-doped Ce–N–TiO_2, Ce–C–TiO_2, and Ce–B–TiO_2 exhibited Type II isotherm with H3 hysteresis loop corresponding to slit-shaped pores (Fig. 2b). For sulfur co-doped sample, H1 hysteresis loop was observed, which indicated the presence of open cylindrical pores. Figure 2b shows that the pore size distribution varied significantly with nonmetals. For Ce–N–TiO_2 and Ce–B–TiO_2, narrow pore distribution was obtained, with 39 and 47 % pores being below 10 nm, respectively. The pore size distributions of Ce–C–TiO_2 and Ce–S–TiO_2 co-doped samples were much broader. The presence of significant amount of pores in the range of 20–50 nm may have contributed to their lower surface area. The surface area and pore size distribution results showed that the presence of nonmetal had significant effect on the stabilization of porous network. The maximum effect was observed for Ce–N–TiO_2 with highest surface area.
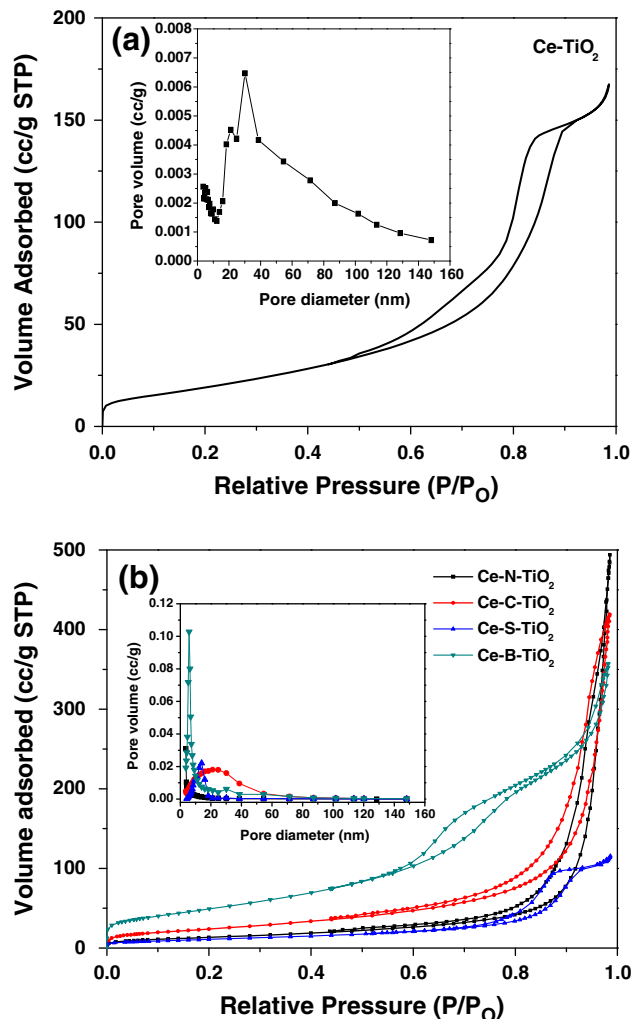
Fig. 2 N_2 adsorption–desorption isotherms of Ce–TiO_2 and Ce–NM–TiO_2 (NM = B, C, N, S) samples (*inset* pore size distribution)

The X-ray diffraction patterns of Ce–TiO_2 and Ce–NM–TiO_2 are shown in Fig. 3. All the samples, except Ce–N–TiO_2, were dominated by anatase phase ($2\theta = 25.5°$, 37°, 48°, 53.8°, 55.1°, 64°, JCPDS 21-1272). For Ce–N–TiO_2, significant amount of rutile phase ($2\theta = 28°$, 36.1°, 41.5°, JCPDS 21-1276) was observed. In general, the phase transformation of anatase to rutile occurs at temperature above 873 K and anatase phase is expected to be dominant in samples calcined at lower temperature of 723 K, used in this study. Accordingly, anatase phase was dominant in XRD profiles of all samples except Ce–N–TiO_2. For Ce–N–TiO_2 sample, the presence of significant amount of rutile phase suggests that nitrogen can catalyzes the anatase–rutile phase transformation significantly at lower temperature [23]. In addition, Ce–S–TiO_2 co-doped sample was more amorphous in nature as observed from broad XRD peaks of low intensity compared to that of other nonmetal-doped samples. No characteristic peaks of CeO_2
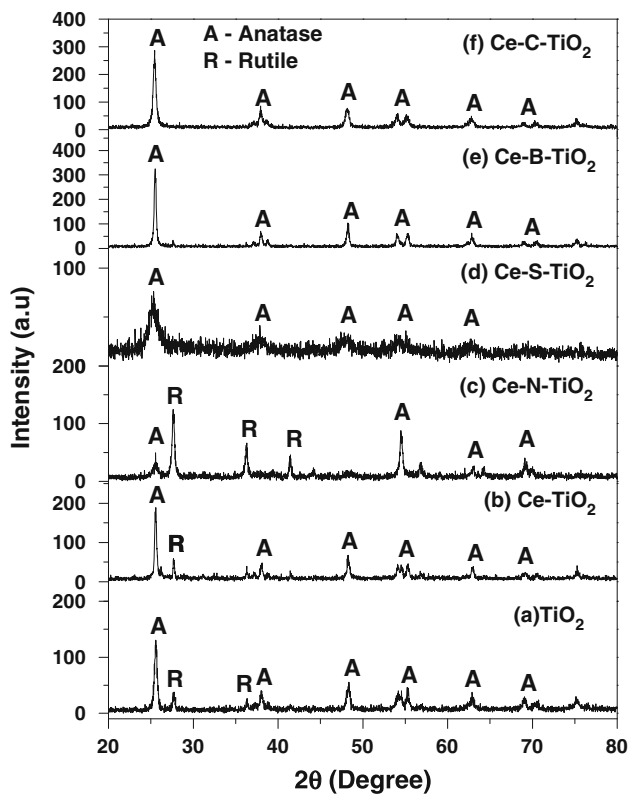
Fig. 3 XRD patterns of TiO_2, $Ce–TiO_2$, and $Ce–NM–TiO_2$ (NM = B, C, N, S) samples

phases were observed in the XRD profiles, which suggest that the ceria was well dispersed in TiO_2 matrix or were below detection limit. In addition, no peaks due to any Ce–Ti mixed oxides were observed in any of the samples.

On addition of Ce to TiO_2, cerium ions can substitute Ti^{4+} sites or can occupy the interstitial sites with Ce–O–Ti linkages [24]. But this is expected to be associated with distortion in titania lattice due to larger size of Ce^{4+} (IR = 0.101 nm) and Ce^{3+} (IR = 0.111 nm) compared to Ti^{4+} (IR = 0.068 nm) ions. The lattice distortion values are shown in Table 1 and correspond to maximum strain observed in crystal lattice due to distortion by incorporation of dopant metals. The lattice distortion was calculated using the formula defined by Stokes and Wilson as $\varepsilon = \beta/(4 \tan \theta)$, where β is the full width at half maximum of diffracted peaks and θ is the Bragg angle of the [h k l] reflection [25]. Maximum value of lattice distortion was obtained, as expected for $Ce–S–TiO_2$ sample, since sulfur has largest ionic radii among the nonmetals used. The corresponding change in lattice parameters for tetragonal titania lattice is also included in Table 1. With the addition of Ce in TiO_2, due to the lattice distortion, the lattice parameters increased compared to that of undoped titania. Co-addition of nonmetals resulted in further increase in lattice parameter values.

The FESEM images of undoped TiO_2, $Ce–TiO_2$, $Ce–NM–TiO_2$ are shown in Fig. 4. The images showed a

definite change in morphology of the samples when cerium and nitrogen were added to titania suggesting that the dopants played a prominent role in the development of material structure during co-precipitation. This resulted in different physical properties as was observed in Table 1. Particles of irregular shape and size were observed for undoped titania, whereas ceria-doped titania, prepared by co-precipitation, consisted of particles of regular size and shape. The particles were spherical in the range of 100–200 nm. The morphology again changed when titania was co-doped with cerium and nonmetals. All the co-doped $Ce–NM–TiO_2$ samples were agglomerated in nature.

The UV–Visible absorption spectra of TiO_2, $Ce–TiO_2$, and $Ce–NM–TiO_2$ are shown in Fig. 5. The $Ce–TiO_2$ sample showed intense absorption bands in the visible light region ranging from 400 to 500 nm. The band gap energies of the samples were determined by extrapolating the rising part of the onset of the absorption edge to the x-axis (λ, nm). The values of λ was then used in the Planck's Einstein equation to calculate the band gap, $E_g = hc/\lambda$, where E_g is band gap energy in eV, h is Planck's constant in eV. s, c is the speed of light in m/s, and λ is the absorption wavelength in nm [26]. The calculated band gap energy values for undoped TiO_2 and $Ce–TiO_2$ were 3.11, and 2.81, respectively. The decreased band gap energy values of cerium-doped sample indicated the formation of new energy levels within the TiO_2 band gap and resulted in redshift of the absorption edge. This shift can be attributed to the incorporation of Ce 4f levels into the TiO_2 crystal structure just below the conduction band of TiO_2 and thereby reducing the effective band gap [27]. Addition of nonmetal to cerium-doped TiO_2 samples resulted in further shift in the band gap energy to longer wavelength. Significant reductions in the optical band gap energies from 3.11 eV for undoped TiO_2 to about 2.88 eV for $Ce–B–TiO_2$, 2.66 eV for $Ce–C–TiO_2$, 2.29 eV for $Ce–N–TiO_2$, and 2.24 eV for $Ce–S–TiO_2$ were observed for co-doped samples. For the co-doped catalysts, the band gap energy was affected by the formation of additional impurity states within titania matrix by the interaction of p-orbitals of the nonmetal dopants (B, C, N, S) and 2p-orbitals of oxygen [28–31]. The relative position of the new states with respect to valence band of titania depends on the properties of dopants and its position within the matrix. Whether the nonmetal dopant would occupy anionic or cationic substitutional sites or interstitial site depends upon its size, chemical valence and electronegativity compared that of the host TiO_2. The probability that a dopant will substitute oxygen depends on its electronegativity [32]. As difference in electronegativity values of dopant and oxygen becomes smaller, the probability that dopant will substitute oxygen becomes higher. Substitutional dopants form the new band states at higher energy level compared to interstitial dopant
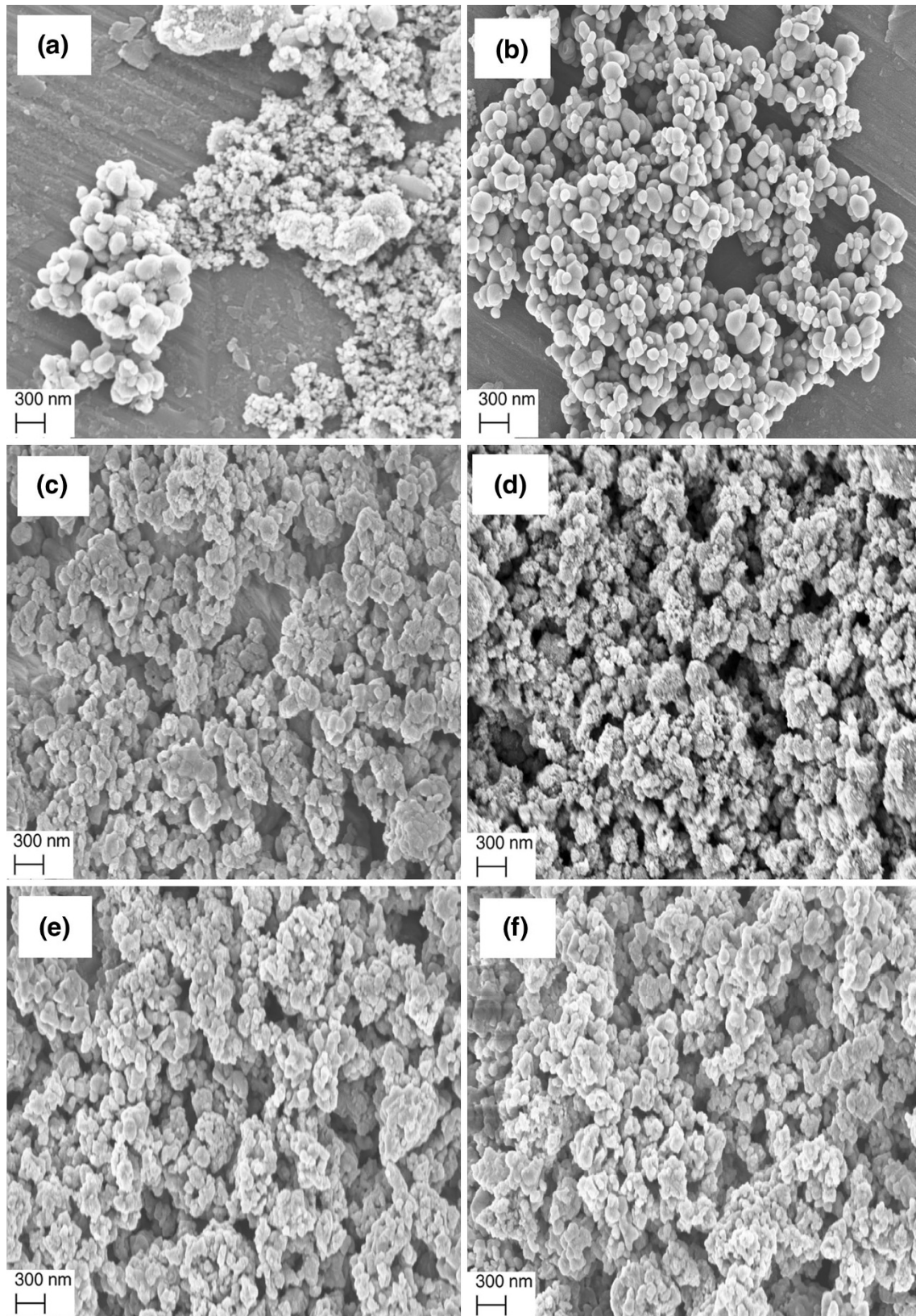
Fig. 4 FESEM images of samples **a** TiO_2, **b** Ce–TiO_2, **c** Ce–N–TiO_2, **d** Ce–S–TiO_2, **e** Ce–B–TiO_2, and **f** Ce–C–TiO_2
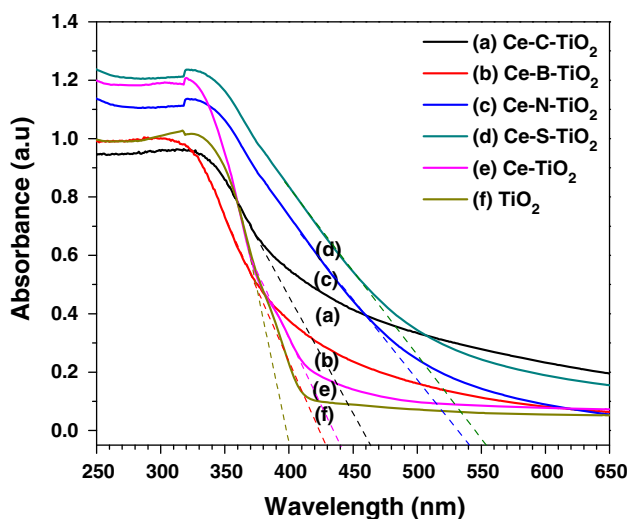
Fig. 5 UV–Visible diffuse reflectance spectra of TiO_2, Ce–TiO_2, and Ce–NM–TiO_2 (NM = B, C, N, S) samples

Fig. 6 Photoluminescence spectra of TiO_2, Ce–TiO_2, and Ce–NM–TiO_2 (NM = B, C, N, S) samples

[33]. For boron co-doped catalyst, it is difficult to replace Ti^{4+} sites by B^{3+} due to the smaller ionic radius of B^{3+} (IR = 0.023 nm) compared to Ti^{4+} (IR = 0.068 nm). Therefore, boron may replace either an oxygen atom or incorporate in the interstitial position in TiO_2 matrix. But due to the lower electronegativity of boron, its probability of occupying the interstitial sites is higher. Similarly, carbon can also substitute oxygen or occupy an interstitial site. In nitrogen co-doped sample, the substitution of oxygen sites is most probable due to their closer electronegativity values [34]. Substitutions of S in both anionic and cationic sites of TiO_2 have been reported in the literature [35, 36]. However, anionic sulfur substitution by S^{2-} (IR = 0.17 nm) might be difficult because of its larger ionic radius than O^{2-} (IR = 0.122 nm). But the cationic substitution of Ti^{4+} (IR = 0.068 nm) by S^{6+} (IR = 0.029 nm) would be more favorable due to smaller size of latter. When TiO_2 is doped with sulfur, either the mixing of S $3p$ states with valence band O $2p$ states or the formation of isolated p-orbitals of S above the valence band maximum of TiO_2 contributes toward narrowing the band gap [37].

The radiative recombination of electron–hole pairs in photocatalysts can be studied by the photoluminescence (PL) emission spectra. Figure 6 shows the room-temperature photoluminescence spectra of the TiO_2, Ce–TiO_2, and Ce–NM–TiO_2 samples in the range of 350–600 nm. For all the samples, six emission peaks appeared at 360, 396, 450, 468, 481, and 492 nm wavelengths and the corresponding transition energy are 3.44, 3.13, 2.76, 2.65, 2.8, and 2.52 eV, respectively. In the literature, the peak in the range of 360–370 nm has been assigned to either anatase particle <10 nm [38] or to self-trapped excitons localized in TiO_6 octahedral [39]. In this study, the emission peak at
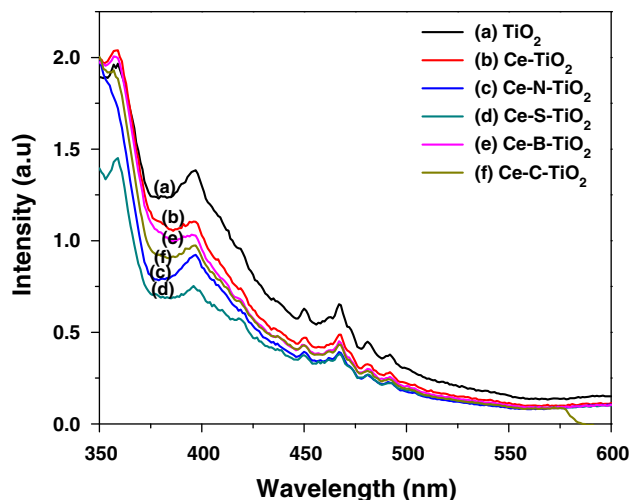
360 nm can be ascribed to the latter as particle is much larger than 10 nm. The emission signal at 396 nm (3.13 eV) corresponds to the band gap transition of the anatase [38]. This agrees well with the band gap energy of titania calculated from UV–Vis spectra. The excitonic emissions in titania result due to the presence of defects and oxygen vacancies. The bands at 450 and 468 nm can be attributed to free excitons, and emission peaks at longer wavelength of 481 and 492 nm can be attributed to the bound excitons [40, 41]. The bound excitons result due to the presence of oxygen vacancies [40, 42, 43]. It can be observed from the Fig. 6 that Ce–TiO_2 had lower PL intensity compared to TiO_2. In Ce–TiO_2, cerium dopant-induced energy level in TiO_2 band structure, as discussed earlier, serves as an electron trap as represented by Eq. (1) resulting in non-radiative recombinations.

$$Ce^{4+} + e^- \rightarrow Ce^{3+} \qquad (1)$$

This reduces the rate of radiative recombination of photogenerated electrons with holes in valence band of titania as shown in Fig. 6. The PL emission intensities of the cerium and nonmetal co-doped samples decreased in the order of TiO_2 > Ce–TiO_2 > Ce–B–TiO_2 > Ce–C–TiO_2 > Ce–N–TiO_2 > Ce–S–TiO_2. In the cerium and nonmetal co-doped samples, the oxygen vacancies generated by substituting nonmetal dopants can act as additional effective traps for photo-induced electrons, thereby reducing the radiative recombination rate of charge carriers further. The photogenerated electrons are trapped by oxygen vacancies by non-radiative combinations [42]. The decreasing emission intensity order can be attributed to increased oxygen vacancies resulted by increasing substitution effects from B to N as discussed in earlier section. In sulfur co-doped samples, the
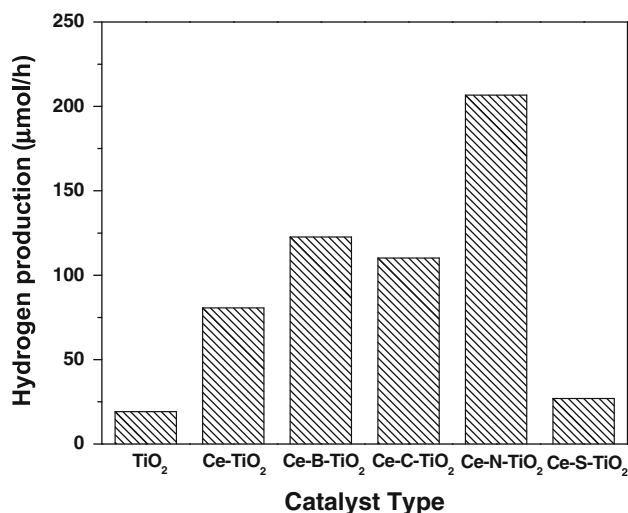
Fig. 7 Hydrogen evolution over TiO_2, $Ce–TiO_2$, and $Ce–NM–TiO_2$ (NM = B, C, N, S) samples

Fig. 8 Schematic representation of hydrogen production over cerium and nonmetal co-doped TiO_2 photocatalysts

presence of isolated cationic S^{6+} dopant state may further act as surface trap states for photogenerated electrons, thereby resulting in a significant decrease in the recombination rate and lowering the PL emission.

Photocatalytic activity studies

The photocatalytic hydrogen production from water–methanol mixture for TiO_2, $Ce–TiO_2$, and $Ce–NM–TiO_2$ (NM = B, C, N, S) catalysts is shown in Fig. 7. The activity of undoped TiO_2 was very low but $Ce–TiO_2$ showed significant photocatalytic activity and high hydrogen evolution. The high activity of cerium-doped TiO_2 can be attributed to their ability of absorption of light in visible light region as shown in Fig. 5. Addition of nonmetals such as B, C, and N to $Ce–TiO_2$ samples further enhanced hydrogen evolution activity. This may be attributed to higher surface area, enhanced visible light absorption as well as lower recombination rate of electron–hole pairs in co-doped samples. The highest activity of $Ce–N–TiO_2$ among co-doped samples may be attributed to its higher surface area, higher visible light absorption, and lower recombination rate of electron–hole pairs compared to other nonmetals, B and C, doped samples. The activity of $Ce–C–TiO_2$ should be higher than $Ce–B–TiO_2$ due to higher absorption of visible light and lower recombination of photogenerated electron–hole pairs for former as shown by absorption spectra (Fig. 5) and PL spectra (Fig. 6), respectively. But slightly higher hydrogen evolution observed for $Ce–B–TiO_2$ compared to that of $Ce–C–TiO_2$ may be attributed to higher surface area of former providing more active sites. Much lower hydrogen production was observed for $Ce–S–TiO_2$ sample, although it has enhanced absorption in the visible light region and efficient
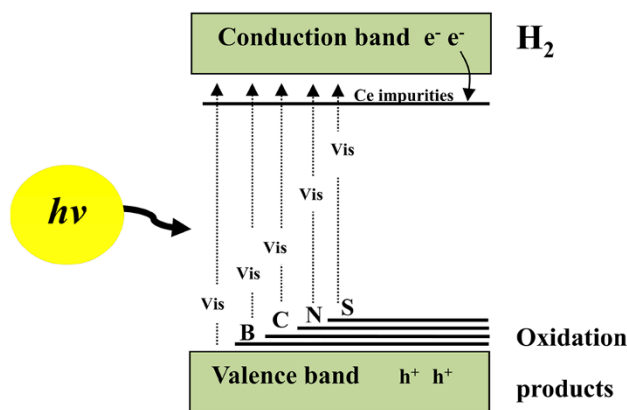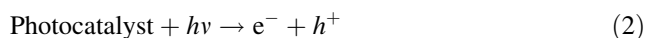
charge separation. The lower activity of $Ce–S–TiO_2$ can be attributed to its very low surface area. Moreover, the S may be in isolated state and that may lead to lower mobility of the holes and limits the number of charge carriers reaching the catalyst surface. This may have also resulted in lower photocatalytic activity in S-doped samples.

The apparent quantum efficiency of the photocatalysts was calculated using the method followed by Sasikala et al. [44]. The apparent quantum efficiency values of TiO_2, $Ce–TiO_2$, $Ce–B–TiO_2$, $Ce–C–TiO_2$, $Ce–N–TiO_2$, and $Ce–S–TiO_2$ were 1.6, 6.7, 10.2, 9.2, 17.2, and 2.2 %, respectively. The calculated values agreed with the reported apparent quantum efficiency range of 2–22 % for different photocatalysts [45]. For comparison, the photocatalytic activity of $N–TiO_2$ was also measured. The apparent quantum efficiency of $N–TiO_2$ (8.6 %) was slightly higher than that $Ce–TiO_2$ (6.7 %) but the efficiency increased significantly for co-doped $Ce–N–TiO_2$ to 17.2, suggesting that both doping components were contributory to photocatalytic activity, as discussed earlier, giving higher hydrogen production. The results are shown in Supplementary Figure S2.

The durability test of $Ce–N–TiO_2$ for photocatalytic H_2 production from water–methanol mixture was performed for 10 h irradiation period with hydrogen evolution being recorded at every 1 h as shown in Figure S3 of supplementary information. The total hydrogen evolution of 737 µmol was obtained after 10 h of irradiation time. The observed results showed that the $Ce–N–TiO_2$ had high H_2 evolution rate as well as desired durability.

Based on the observed band gap energies of co-doped samples, the position of the impurity states and probable transitions of electrons are schematically shown in Fig. 8. In $Ce–TiO_2$, the photogenerated electrons are excited from the valence band to extended conduction band where electrons are trapped effectively by Ce^{4+}/Ce^{3+} couple. This results in the accumulation of electrons in extended
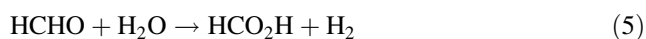
conduction band, which can serve as hydrogen formation site. On addition of nonmetals to cerium-doped titania, the excitation of electrons can also takes place from nonmetal-induced impurity levels resulting in the absorption of visible light. The reduction and oxidation reactions occurring in conduction band and valance band, respectively, can be represented as follows [46, 47].

$$Photocatalyst + h\nu \rightarrow e^- + h^+ \tag{2}$$

Reduction reaction

$$2e_{cb}^- + 2H^+ \rightarrow H_2 \tag{3}$$

Oxidation reactions:

$$CH_3OH + 2h_{vb}^+ \rightarrow 2H^+ + HCHO \tag{4}$$

$$HCHO + H_2O \rightarrow HCO_2H + H_2 \tag{5}$$

$$HCO_2H + h_{vb}^+ \rightarrow CO_2 + H^+ \tag{6}$$

In addition to proposed hole-mediated path as shown in the above reaction scheme, methanol can also enhances hydrogen generation by reacting with hydroxyl radicals generated from photocatalytic water splitting [48]. The oxidation of methanol results in the formation of HCHO, HCOOH, and CO_2. For oxidation of formaldehyde to formic acid, the extra oxygen atom is provided by water through hydroxyl radical. Intermediate products were only detected in liquid phase, and no intermediate products were detected in gaseous phase in the present study.

Conclusions

Cerium and nonmetal co-doped samples synthesized by co-precipitation method were found to be potential photocatalysts for hydrogen generation under visible light radiation. Doping of titania with cerium induced distinct redshift of the absorption edge in visible light region. Nonmetal modification further enhanced the visible light absorption and separation efficiency of photogenerated electron–hole pairs. The effective band gap energies of co-doped samples depended on the properties of nonmetals. The surface area and phase distribution were also modified in the presence of nonmetal. Highest hydrogen evolution rate of 206 μmol/h was observed for cerium–nitrogen co-doped sample. The higher photoactivty of Ce–N–TiO_2 can be attributed to higher surface area, higher light absorption, and efficient charge separation.

References

1. Ashokkumar, M.: An overview on semiconductor particulate systems for photoproduction of hydrogen. Int. J. Hydrog. Energy **23**, 427–438 (1998)
2. Balat, H., Kirtay, E.: Hydrogen from biomass—present scenario and future prospects. Int. J. Hydrog. Energy **35**, 7416–7426 (2010)
3. Holladay, J.D., Hu, J., King, D.L., Wang, Y.: An overview of hydrogen production technologies. Catal. Today **139**, 244–260 (2009)
4. Kudo, A.: Photocatalysis and solar hydrogen production. Pure Appl. Chem. **79**, 1917–1927 (2007)
5. Takata, T., Tanaka, A., Hara, M., Kondo, J.N., Domen, K.: Recent progress of photocatalysts for overall water splitting. Catal. Today **44**, 17–26 (1998)
6. Gurunathan, K., Maruthamuthu, P.: Photogeneration of hydrogen using visible light with undoped/doped α-Fe_2O_3 in the presence of methyl viologen. Int. J. Hydrog. Energy **20**, 287–295 (1995)
7. Wang, X., Liu, G., Lu, G.Q., Cheng, H.-M.: Stable photocatalytic hydrogen evolution from water over ZnO–CdS core–shell nanorods. Int. J. Hydrog. Energy **35**, 8199–8205 (2010)
8. Kudo, A., Miseki, Y.: Heterogeneous photocatalyst materials for water splitting. Chem. Soc. Rev. **38**, 253–278 (2009)
9. Ni, M., Leung, M.K.H., Leung, D.Y.C., Sumathy, K.: A review and recent developments in photocatalytic water-splitting using TiO_2 for hydrogen production. Renew. Sustain. Energy Rev. **11**, 401–425 (2007)
10. Pelaez, M., Nolan, N.T., Pillai, S.C., Seery, M.K., Falaras, P., Kontos, A.G., Dunlop, P.S.M., Hamilton, J.W.J., Byrne, J.A., O'Shea, K., Entezari, M.H., Dionysiou, D.D.: A review on the visible light active titanium dioxide photocatalysts for environmental applications. Appl. Catal. B **125**, 331–349 (2012)
11. Xu, A., Gao, Y., Liu, H.: The preparation, characterization, and their photocatalytic activities of rare-earth-doped TiO_2 nanoparticles. J. Catal. **207**, 151–157 (2002)
12. Tong, T., Zhang, J., Tian, B., Chen, F., He, D., Anpo, M.: Preparation of Ce–TiO_2 catalysts by controlled hydrolysis of titanium alkoxide based on esterification reaction and study on its photocatalytic activity. J. Colloid Interface Sci. **315**, 382–388 (2007)
13. Silva, A.M.T., Silva, C.G., Drazic, G., Faria, J.L.: Ce-doped TiO_2 for photocatalytic degradation of chlorophenol. Catal. Today **144**, 13–18 (2009)
14. Fan, C., Xue, P., Sun, Y.: Preparation of nano-TiO_2 doped with cerium and its photocatalytic activity. J. Rare Earths **24**, 309–313 (2006)
15. Asahi, R., Morikawa, T., Ohwaki, T., Aoki, K., Taga, Y.: Visible-light photocatalysis in nitrogen-doped titanium oxides. Science **293**, 269–271 (2001)
16. Ohno, T., Akiyoshi, M., Umebayashi, T., Asai, K., Mitsui, T., Matsumura, M.: Preparation of S-doped TiO_2 photocatalysts and their photocatalytic activities under visible light. Appl. Catal. A **265**, 115–121 (2004)
17. Yun, H.J., Lee, H., Joo, J.B., Kim, N.D., Kang, M.Y., Yi, J.: Facile preparation of high performance visible light sensitive photo-catalysts. Appl. Catal. B **94**, 241–247 (2010)
18. Shen, X.Z., Liu, Z.C., Xie, S.M., Guo, J.: Degradation of nitrobenzene using titania photocatalyst co-doped with nitrogen and cerium under visible light illumination. J. Hazard. Mater. **162**, 1193–1198 (2009)
19. Huang, D.G., Liao, S.J., Zhou, W.B., Quan, S.Q., Liu, L., He, Z.J., Wan, J.B.: Synthesis of samarium- and nitrogen-co-doped TiO_2 by modified hydrothermal method and its photocatalytic performance for the degradation of 4-chlorophenol. J. Phys. Chem. Solids **70**, 853–859 (2009)

20. Moon, S.-C., Mametsuka, H., Tabata, S., Suzuki, E.: Photocatalytic production of hydrogen from water using TiO_2 and B/TiO_2. Catal. Today **58**, 125–132 (2000)

21. Khan, S.U.M., Al-Shahry, M., Ingler Jr, W.B.: Efficient photochemical water splitting by a chemically modified n-TiO_2. Science **297**, 2243–2245 (2002)

22. Sreethawong, T., Laehsalee, S., Chavadej, S.: Comparative investigation of mesoporous- and non-mesoporous-assembled TiO_2 nanocrystals for photocatalytic H_2 production over N-doped TiO_2 under visible light irradiation. Int. J. Hydrog. Energy **33**, 5947–5957 (2008)

23. Sidheswaran, M., Tavlarides, L.L.: Characterization and visible light photocatalytic activity of cerium- and iron-doped titanium dioxide sol–gel materials. Ind. Eng. Chem. Res. **48**, 10292–10306 (2009)

24. Yu, T., Tan, X., Zhao, L., Yin, Y., Chen, P., Wei, J.: Characterization, activity and kinetics of a visible light driven photocatalyst: cerium and nitrogen co-doped TiO_2 nanoparticles. Chem. Eng. J. **157**, 86–92 (2010)

25. Llordés, A., Palau, A., Gázquez, J., Coll, M., Vlad, R., Pomar, A., Arbiol, J., Guzmán, R., Ye, S., Rouco, V., et al.: Nanoscale strain-induced pair suppression as a vortex-pinning mechanism in high-temperature superconductors. Nat. Mater. **11**, 329–336 (2012)

26. Sreethawong, T., Suzuki, Y., Yoshikawa, S.: Synthesis, characterization, and photocatalytic activity for hydrogen evolution of nanocrystalline mesoporous titania prepared by surfactant-assisted templating sol–gel process. J. Solid State Chem. **178**, 329–338 (2005)

27. Magesh, G., Viswanathan, B., Viswanath, R.P., Varadarajan, T.K.: Photocatalytic behavior of CeO_2–TiO_2 system for the degradation of methylene blue. Indian J. Chem. **48A**, 480–488 (2009)

28. Zhao, W., Ma, W., Chen, C., Zhao, J., Shuai, Z.: Efficient degradation of toxic organic pollutants with $Ni_2O_3/TiO_{2-x}B_x$ under visible irradiation. J. Am. Chem. Soc. **126**, 4782–4783 (2004)

29. Sathish, M., Viswanathan, B., Viswanath, R.P.: Characterization and photocatalytic activity of N-doped TiO_2 prepared by thermal decomposition of Ti–melamine complex. Appl. Catal. B **74**, 307–312 (2007)

30. Yu, C., Yu, J.C.: A simple way to prepare C–N-codoped TiO2 photocatalyst with visible-light activity. Catal. Lett. **129**, 462–470 (2009)

31. Tian, F., Liu, C., Zhao, W., Wang, X., Wang, Z., Yu, J.C.: Cationic S-doped anatase TiO_2: a DFT study. J. Comput. Sci. Eng. **1**, 33–41 (2011)

32. Lu, J., Jin, H., Dai, Y., Yang, K., Huang, B.: Effect of electronegativity and charge balance on the visible-light-responsive photocatalytic activity of nonmetal doped anatase TiO_2. Int. J. Photoenergy. Article ID 928503, 8 pp (2012)

33. Di Valentin, C., Pacchioni, G.: Trends in non-metal doping of anatase TiO_2: B, C, N and F. Catal. Today **206**, 12–18 (2013)

34. Kitano, M., Matsuoka, M., Ueshima, M., Anpo, M.: Recent developments in titanium oxide-based photocatalysts. Appl. Catal. A **325**, 1–14 (2007)

35. Umebayashi, T., Yamaki, T., Itoh, H., Asai, K.: Band gap narrowing of titanium dioxide by sulfur doping. Appl. Phys. Lett. **81**, 454–456 (2002)

36. Yu, J.C., Ho, W., Yu, J., Yip, H., Wong, P.K., Zhao, J.: Efficient visible-light-induced photocatalytic disinfection on sulfur-doped nanocrystalline titania. Environ. Sci. Technol. **39**, 1175–1179 (2005)

37. Xiang, Q., Yu, J., Jaroniec, M.: Nitrogen and sulfur co-doped TiO2 nanosheets with exposed 001 facets: synthesis, characterization and visible-light photocatalytic activity. Phys. Chem. Chem. Phys. **13**, 4853–4861 (2011)

38. Li, Y., Lee, N.-H., Hwang, D.-S., Song, J.S., Lee, E.G., Kim, S.-J.: Synthesis and characterization of nano titania powder with high photoactivity for gas-phase photo-oxidation of benzene from $TiOCl_2$ aqueous solution at low temperatures. Langmuir **20**, 10838–10844 (2004)

39. Hu, C., Zhang, R., Xiang, J., Liu, T., Li, W., Li, M., Duo, S., Wei, F.: Synthesis of carbon nanotube/anatase titania composites by a combination of sol–gel and self-assembly at low temperature. J. Solid State Chem. **184**, 1286–1292 (2011)

40. Yu, J., Hai, Y., Jaroniec, M.: Photocatalytic hydrogen production over CuO-modified titania. J. Colloid Interface Sci. **357**, 223–228 (2011)

41. Zhang, Y.X., Li, G.H., Jin, Y.X., Zhang, Y., Zhang, J., Zhang, L.D.: Hydrothermal synthesis and photoluminescence of TiO_2 nanowires. Chem. Phys. Lett. **365**, 300–304 (2002)

42. Wang, E., Yang, W., Cao, Y.: Unique surface chemical species on indium doped TiO_2 and their effect on the visible light photocatalytic activity. J. Phys. Chem. C **113**, 20912–20917 (2009)

43. Selvam, K., Balachandran, S., Velmurugan, R., Swaminathan, M.: Mesoporous nitrogen doped nano titania—a green photocatalyst for the effective reductive cleavage of azoxybenzenes to amines or 2-phenyl indazoles in methanol. Appl. Catal. A **413–414**, 213–222 (2012)

44. Sasikala, R., Sudarsan, V., Sudakar, C., Naik, R., Sakuntala, T., Bharadwaj, S.R.: Enhanced photocatalytic hydrogen evolution over nanometer sized Sn and Eu doped titanium oxide. Int. J. Hydrog. Energy **33**, 4966–4973 (2008)

45. Jin, Z., Zhang, X., Li, Y., Li, S., Lu, G.: 5.1% Apparent quantum efficiency for stable hydrogen generation over eosin-sensitized CuO/TiO_2 photocatalyst under visible light irradiation. Catal. Commun. **8**, 1267–1273 (2007)

46. Wu, N.-L., Lee, M.-S.: Enhanced TiO_2 photocatalysis by Cu in hydrogen production from aqueous methanol solution. Int. J. Hydrog. Energy **29**, 1601–1605 (2004)

47. Choi, H.-J., Kang, M.: Hydrogen production from methanol/water decomposition in a liquid photosystem using the anatase structure of Cu loaded TiO_2. Int. J. Hydrog. Energy **32**, 3841–3848 (2007)

48. Chiarello, G.L., Ferri, D., Selli, E.: Effect of the CH_3OH/H_2O ratio on the mechanism of the gas-phase photocatalytic reforming of methanol on noble metal-modified TiO_2. J. Catal. **280**, 168–177 (2011)